

University of South Dakota

USD RED

Honors Thesis

Theses, Dissertations, and Student Projects

5-2021

ELECTRONIC STRUCTURE AND DYNAMICS OF URANYL- PEROXIDE SPECIES

Ethan T. Hare

Follow this and additional works at: <https://red.library.usd.edu/honors-thesis>

Part of the [Chemistry Commons](#)

Commons

Network

Logo

ELECTRONIC STRUCTURE AND DYNAMICS OF URANYL-PEROXIDE SPECIES

by

Ethan T. Hare

A Thesis Submitted in Partial Fulfillment

Of the Requirements for the

University Honors Program

Department of Chemistry

The University of South Dakota

May 2021

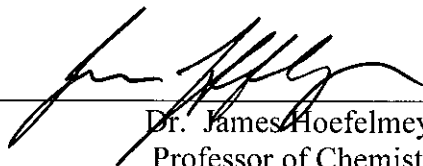
The members of the Honors Thesis Committee appointed
to examine the thesis of Ethan T. Hare
find it satisfactory and recommend that it be accepted.



Dr. Pere Miro
Assistant Professor of Chemistry
Director of the Committee



Dr. Bess Vlajsavljevich
Assistant Professor of Chemistry



Dr. James Hoefelmeyer
Professor of Chemistry

ABSTRACT

Electronic Structure and Dynamics of Uranyl-Peroxide Species

Ethan T. Hare

Director: Pere Miro, Ph.D.

Uranyl-peroxide nanocapsules are a unique family of self-assembled actinide species. Uranyl ions rapidly self-assemble in basic peroxidic media through a myriad of reactions to coalesce into a single nanocapsule that includes both peroxide and hydroxide bridging groups between the uranyl moieties. A wide variety of capsules can be formed, and it has been proposed that square and pentagonal building blocks assemble prior to nanocapsule formation. We have studied the speciation of the pentagonal $[(U^{VI}O_2)_5(\eta^2-O_5)_5(\mu-\eta^2, \eta^2-O_2)_{5-n}(OH)_{2n}]^{10-}$ uranyl-peroxide nanocapsule building blocks using density functional theory calculations. We predicted the most favorable speciation pathways for the self-assembly of the building blocks prior to cluster formation including the effect of pH, temperature, and alkali counterions. In addition, we also mapped the potential energy surface by scanning the molecular normal modes and created a large database containing uranyl monomers $[(UO_2)(\eta^2-O_2)_3]^+$ and $[(UO_2)(\eta^2-O_2)_2(OH)]^3-$. We then used the atomistic machine learning package to train a neural network potential in order to create a cheap structure-energy connection that could be used to predict quantum mechanics energetics of larger uranyl-peroxide systems for a fraction of the computational cost.

KEYWORDS: nuclear fuel cycle, uranyl-peroxide, nanocapsules, density functional theory, speciation, machine learning

TABLE OF CONTENTS

Acronym List	v
List of Figures	vi
List of Tables	viii
Acknowledgements	ix
Chapter One: Introduction	1
Chapter Two: Computational Details	5
Quantum Chemical Calculations	5
Neural Network	6
Chapter Three: Results	8
Speciation of Pentagonal [(U^{VI}O₂)₅(η²-O₅)₅(μ-η²,η²-O₂)_{5-n}(OH)_{2n}]¹⁰⁻ Uranyl- Peroxide Species	8
Electrostatic Potentials	11
Neural Network Potentials	14
Chapter Four: Conclusions	18
References	19

ACRONYM LIST

Density functional theory, DFT; Amsterdam Density Functional, ADF2017; Perdew-Burke-Ernzerhof, PBE; Slater-type triple-z plus a polarization function, TZP; zero-order regular approximation, ZORA; conductor-like screening model, COSMO; neural network potential, NNP; atomistic machine-learning package, AMP; root mean square error, RMSE; HOMO, highest occupied molecular orbital; DoS, density of states.

LIST OF FIGURES

Figure 1	2
Water radiolysis by a, b, and g radiation present in spent nuclear fuel rods and its role in the solubilization of uranium oxide rods.	
Figure 2	3
Example of uranyl-peroxide nanoclusters synthesis from uranyl ($[U^{VI}O_2]^{2+}$), a base (XOH), and hydrogen peroxide (H_2O_2).	
Figure 3	4
Geometry and schematic representation $[(UO_2)_5(\eta^2-O_2)_5(\mu-\eta^2, \eta^2-O_2)_5]^{10-}$ (left) and $[(UO_2)_5(\eta^2-O_2)_5(\mu-\eta^2, \eta^2-O_2)_3(OH)_4]^{10-}$ (right) uranyl-peroxide species Color code: Uranium in yellow, oxygen in red, and hydrogen in white.	
Figure 4	9
Speciation of pentagonal $[(U^{VI}O_2)_5(\eta^2-O_5)_5(\mu-\eta^2, \eta^2-O_2)_{5-n}(OH)_{2n}]^{10-}$ uranyl-peroxide nanocapsule building blocks at varying conditions.	
Figure 5	10
Speciation of pentagonal $[(U^{VI}O_2)_5(\eta^2-O_5)_5(\mu-\eta^2, \eta^2-O_2)_{5-n}(OH)_{2n}]^{10-}$ uranyl-peroxide nanocapsule building blocks in presence of Na^+ at varying conditions.	
Figure 6	11
Electrostatic potential of $[(UO_2)_5(\eta^2-O_2)_5(\mu-\eta^2, \eta^2-O_2)_5]^{10-}$ and $[(UO_2)_5(\eta^2-O_2)_5(\mu-\eta^2, \eta^2-O_2)_3(OH)_4]^{10-}$ species with and without a Na^+ cation. Density isovalue = 0.04.	
Figure 7	12
HOMO and HOMO-5 molecular orbitals for $[(UO_2)_5(\eta^2-O_2)_5(\mu-\eta^2, \eta^2-O_2)_5]^{10-}$ species and total density for the different DoS peroxide bands.	
Figure 8	13
Density of states (DoS) for the frontier orbitals region of $[(U^{VI}O_2)_5(\eta^2-O_5)_5(\mu-\eta^2, \eta^2-O_2)_{5-n}(OH)_{2n}]^{10-}$ uranyl-peroxide species.	
Figure 9	14
NNP vs DFT energy for the $[(UO_2)(O_2)_3]^{4-}$ test set. NNP was trained using only the training data from the normal mode sampling of $[(UO_2)(O_2)_3]^{4-}$.	
Figure 10	15
NNP vs DFT energy for the $[(UO_2)(O_2)_2(OH)]^{3-}$ test set. NNP was trained using only the training data from the normal mode sampling of $[(UO_2)(O_2)_2(OH)]$.	

Figure 11	15
NNP vs DFT energy for the $[(\text{UO}_2)(\text{O}_2)_3]^{4-}$ and $[(\text{UO}_2)(\text{O}_2)_2(\text{OH})]^{3-}$ test set. NNP was trained using the training data from the normal mode sampling of both monomers.	
Figure 12	17
Power spectra from DFT (black) and NNP (red) for $[(\text{UO}_2)(\text{O}_2)_3]^{4-}$ species. NNP was trained using only the training data from the normal mode sampling of $[(\text{UO}_2)(\text{O}_2)_3]^{4-}$.	

LIST OF TABLES

Table 1.....	16
Comparison between the DFT and NNP energies for different NNP models. Energies in kcal mol ⁻¹ .	

ACKNOWLEDGMENTS

I would like to thank the chemistry department at the University of South Dakota and the South Dakota Board of Regents for providing funding to support summer research experiences. I would especially like to thank Dr. Pere Miro for all his guidance throughout my undergraduate career. All computations supporting this project were performed on High Performance Computing systems at the University of South Dakota funded by NSF (ACI-1626516).

CHAPTER ONE

Introduction

Radioactive waste from the nuclear fuel cycle is one of the most pressing environmental problems of the 21st century. Significant amounts of radioactive waste originate from uranium mining operations and spent nuclear fuel.¹ In the United States, 2,000 tons of radioactive waste is generated every year from nuclear power plants with over 60,000 tons of waste scattered across temporary repositories. Long-term nuclear waste repositories have been proposed at isolated sites such as Yucca Mountain;¹ however, due to the poor public perception of nuclear waste storage, ineffective waste containment, and a lack of federal funding, a long-term repository site has never been fully implemented. This has led to the temporary storage of spent nuclear fuel rods in nuclear power plants before transport to other short-term repositories. The United States nuclear waste problem is further compounded by the lack of nuclear reprocessing facilities which are used by some European countries to reduce the amount of waste to be stored in long-term repositories.

One of the most pressing problems presented by a lack of storing or reprocessing uranium waste is water contamination. The potential for large-scale water contamination became glaringly obvious following the 2011 Fukushima nuclear disaster,² but the risk for groundwater contamination also remains high due to improperly stored uranium mining tailings or spent nuclear fuel waste.^{3 4} Radiation from uranium causes radiolysis of water resulting in the formation of numerous ions and radicals, notably hydroxide radical (Figure 1).⁵ Hydroxide radicals enhance the transformation of solid uranium oxide (spent nuclear fuel rods) into uranium aqueous species via redox reactions, as well as the formation of hydrogen peroxide, oxygen, and hydride ions among other species.⁶

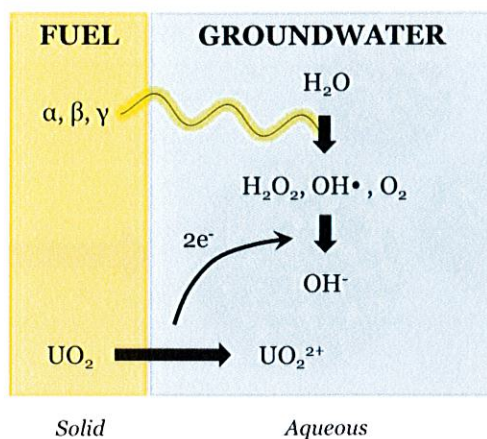


Figure 1. Water radiolysis by α , β , and γ radiation present in spent nuclear fuel rods and its role in the solubilization of uranium oxide rods.

In acidic aqueous media, uranium's most stable form is the uranyl ion, $[\text{U}^{\text{VI}}\text{O}_2]^{2+}$; therefore, the proper understanding of uranyl speciation and chemistry is essential to improving reprocessing and reclamation. Studtite is the only known uranyl peroxide mineral, and it forms when uranyl and peroxide are present in acidic media.^{7,8} The species of interest form in basic pH with H_2O_2 . The uranyl ions rapidly self-assemble into a diverse family of hollow nanoclusters including a large number of uranyl units bridged by peroxide and hydroxide ligands (Figure 2).^{9,10} Uranyl-peroxide species ranging from 20 up to 60 uranyl units have been experimentally isolated with topologies similar to fullerenes. These nanoclusters may have important implications in developing a more efficient nuclear reprocessing cycle involving the filtration of polynuclear nanosized actinide species.¹¹

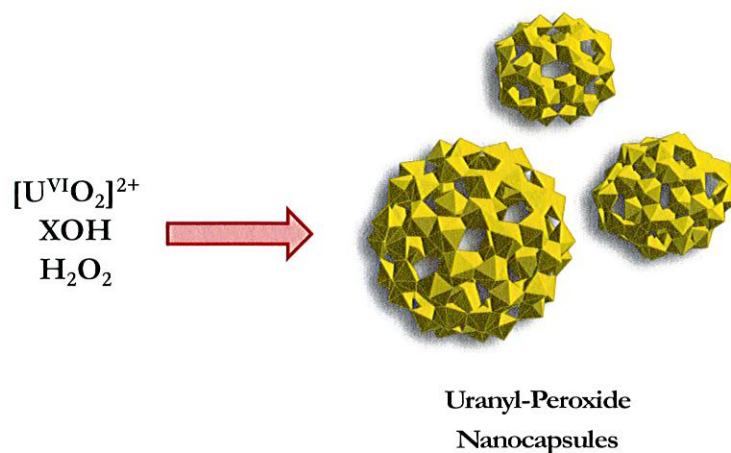


Figure 2. Example of uranyl-peroxide nanoclusters synthesis from uranyl ($[U^{VI}O_2]^{2+}$), a base (XOH), and hydrogen peroxide (H_2O_2).

The exact speciation process from the uranyl ion to the cluster is still unknown, but it is believed the formation of square and/or pentagonal faces occurs first. Several clusters contain only peroxides bridging between the uranyl moieties such as U_{20} , U_{28} , and U_{44} . However, in most cases the speciation of uranyl-peroxide nanocapsules is further complicated by the presence of hydroxide as bridging ligand in addition to peroxide. The ratio of hydroxide/peroxide bridging ligands are strongly affected by the reaction conditions and the nanocapsule itself.¹² Peroxide bridging has a bent dihedral angle of 145.7° and is more flexible than hydroxide bridging which has an almost linear dihedral angle of 173.4° .^{13, 14} Therefore, the peroxide facets are the ones inducing the needed curvature to close the uranyl-peroxide species. Finally, it is also clear that alkali cations mediate in cluster formation, as they control the nuclearity and topology of the final product; however, their exact role still remains unknown beyond the stabilization of the products via ion-pairing.¹⁵⁻¹⁸

In this study, we report our findings on the speciation of pentagonal uranyl peroxide species $[(U^{VI}O_2)_5(\mu-\eta^2, \eta^2-O_2)_{5-n}(\mu-OH)_{2n}(\eta^2-O_2)_5]^{10-}$ ranging from fully peroxide to fully

hydroxide bridging at different experimental conditions using density functional theory calculations. In Figure 3 we present the geometry and schematic representation of two of the studied species: $[(\text{UO}_2)_5(\eta^2\text{-O}_2)_5(\mu\text{-}\eta^2,\eta^2\text{-O}_2)_5]^{10-}$ and $[(\text{UO}_2)_5(\eta^2\text{-O}_2)_5(\mu\text{-}\eta^2,\eta^2\text{-O}_2)_3(\text{OH})_4]^{10-}$. In addition, we have trained a neural network potential to predict the free energy of uranyl monomers as a proof-of-concept for the potential use of neural networks as a method to determine the free energy of larger and more computationally expensive uranyl-peroxide species.

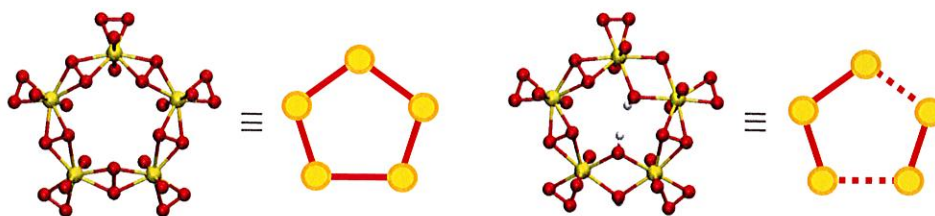


Figure 3. Geometry and schematic representation $[(\text{UO}_2)_5(\eta^2\text{-O}_2)_5(\mu\text{-}\eta^2,\eta^2\text{-O}_2)_5]^{10-}$ (left) and $[(\text{UO}_2)_5(\eta^2\text{-O}_2)_5(\mu\text{-}\eta^2,\eta^2\text{-O}_2)_3(\text{OH})_4]^{10-}$ (right) uranyl-peroxide species. Color code: Uranium in yellow, oxygen in red, and hydrogen in white.

CHAPTER TWO

Computational Details

Quantum Chemical Calculations

All geometries were fully optimized using the density functional theory (DFT) implementation in the Amsterdam Density Functional (ADF2017) package.^{19, 20} The Perdew-Burke-Ernzerhof (PBE) exchange-correlation functional was used in conjunction with a Slater-type triple-z plus a polarization function (TZP) and a small frozen core on all atoms.²¹⁻²³ Relativistic corrections were added using the scalar relativistic zero-order regular approximation (ZORA).^{21, 24, 25} Solvent effects of water were included with the COSMO continuum solvation model.²⁶ The nature of all stationary points was verified by analytic computation of vibrational frequencies which were used for the computation of zero-point vibrational energies and molecular partition functions for use in computing 298.15 K thermal contributions to free energy employing the usual rigid-rotor harmonic oscillator approximation.

Neural Network

The geometries of $[(\text{UO}_2)(\text{O}_2)_3]^{4-}$ and $[(\text{UO}_2)(\text{O}_2)_2(\text{OH})]^{3-}$ were optimized using the above level of theory and the normal mode scan (e.g., the generation of many structures displaced from the energetic minima along each vibrational absorption) was performed by applying stepwise displacements along the harmonic normal modes. Only structures within 1eV of the minimum were considered. This generated a database with 6892 structures for $[(\text{UO}_2)(\text{O}_2)_3]^{4-}$ and a database with 7915 structures for $[(\text{UO}_2)(\text{O}_2)_2(\text{OH})]^{3-}$. The data were randomly divided into a training set and a test set containing 90% and 10% of the structures, respectively. We then trained different neural network potentials (NNPs) with the atomistic machine-learning package (AMP) using either a $[(\text{UO}_2)(\text{O}_2)_3]^{4-}$ or $[(\text{UO}_2)(\text{O}_2)_2(\text{OH})]^{3-}$ training set as well as both of them simultaneously.²⁷

We used atom centered symmetry functions as descriptors of the chemical environment, from which a neural network learns to predict contributions to the total energy or properties. In particular, we used Gaussian functions with different parameters and cutoff radius are employed to describe the local atomic environment to a neural network as proposed by Behler and Parrinello.²⁸ The two-body (G^2) and three body (G^4) symmetry functions (Equation 1 and Equation 2, respectively) describe the radial and angular distribution of neighbor atoms within a cutoff radius respect to any given atom (Equation 3).

$$G_i^2 = \sum_{j \neq i}^N e^{-(hR_{ij}^2)} \cdot f_c(R_{ij}) \quad (1)$$

$$G_i^4 = 2^{1-z} \sum_{j \neq i}^N \sum_{k \neq i, j}^N (1 + \lambda \cos q_{ijk})^z \cdot e^{-h(R_{ij}^2 + R_{ik}^2 + R_{jk}^2)} \cdot f_c(R_{ij}) \cdot f_c(R_{ik}) \cdot f_c(R_{jk}) \quad (2)$$

$$f_c(R_{ij}) = \begin{cases} 0.5 \cdot \left[\cos\left(\frac{pR_{ij}}{R_c}\right) + 1 \right] & \text{for } R_{ij} \leq R_c \\ 0 & \text{for } R_{ij} > R_c \end{cases} \quad (3)$$

where R_{ij} is the distance between atom i and j , R_{ik} is the distance between atom i and k , R_{jk} is the distance between atom j and k , N is the total number of neighbor atoms, f_c is the cutoff function, η , ζ , and λ are Gaussian parameters, and $q_{ijk} = \arccos\left(\frac{R_{ij} \cdot R_{ik}}{R_{ij} \cdot R_{ik}}\right)$. We used a gaussian cutoff of 6.5 angstroms, $G2 = \{\eta = 0.05, 4.0, 20.0, 80.0\}$, $G4 = \{\eta = 0.05; \lambda = 1.0, -1.0; \zeta = 1.0, 4.0\}$, in combination with two hidden layers with 15 neurons. Both energy and forces were used in the NNP training, and the NNP trained until the energy and forces achieved a RMSE of 0.01.

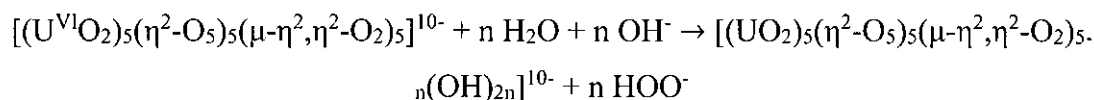
CHAPTER THREE

Results

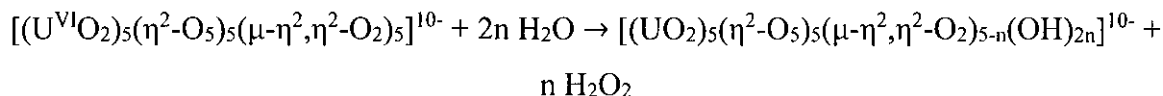
Speciation of Pentagonal $[(U^{VI}O_2)_5(\eta^2-O_5)(\mu-\eta^2,\eta^2-O_2)_{5-n}(OH)_{2n}]^{10-}$ Uranyl-Peroxide Species

We performed geometry optimizations of all possible pentagonal $[(U^{VI}O_2)_5(\eta^2-O_5)(\mu-\eta^2,\eta^2-O_2)_{5-n}(OH)_{2n}]^{10-}$ uranyl-peroxide species with and without the presence of a Na^+ ion pair. We computed their Gibbs free energy of reaction at high pH and peroxide concentration, pH = 14 and $[OOH^-] = 1M$ (Figure 5), and low pH and low peroxide concentration, pH = 8 and $[OOH^-] = 1mM$ (Figure 4). The reaction to transform a bridging peroxide into two hydroxides depends on the pH, since the first pK_a of H_2O_2 is 11.75. We assumed to be the following reactions to compute the speciation of pentagonal uranyl-peroxide species:

pH > 11.75



pH < 11.75



At pH = 14 (Figure 4), only the fully peroxide species is favorable, but the presence of a Na^+ ion pair, species with one and two sets of bridging hydroxides become favorable. It is important to notice that there are isomers for species with 2 and 3 sets of hydroxide bridges, since they can be either consecutive or alternating with peroxide bridges. In all the cases the species with the alternated peroxide/hydroxide bridges is the most stable

isomer. At pH = 8, the fully peroxide species along with the species with one set of bridging hydroxides are favorable; however, the fully peroxide species remains the most favorable one. At pH = 8, with a Na⁺ ion pair, only the species with one and two sets of bridging hydroxides species are favorable. In this case, latter species are the most favorable ones. This demonstrates that the acidification as well as the decrease of hydrogen peroxide in the media (e.g., reaction to form uranyl-peroxide species or decomposition) will impact the speciation of uranyl-peroxide species in solution.

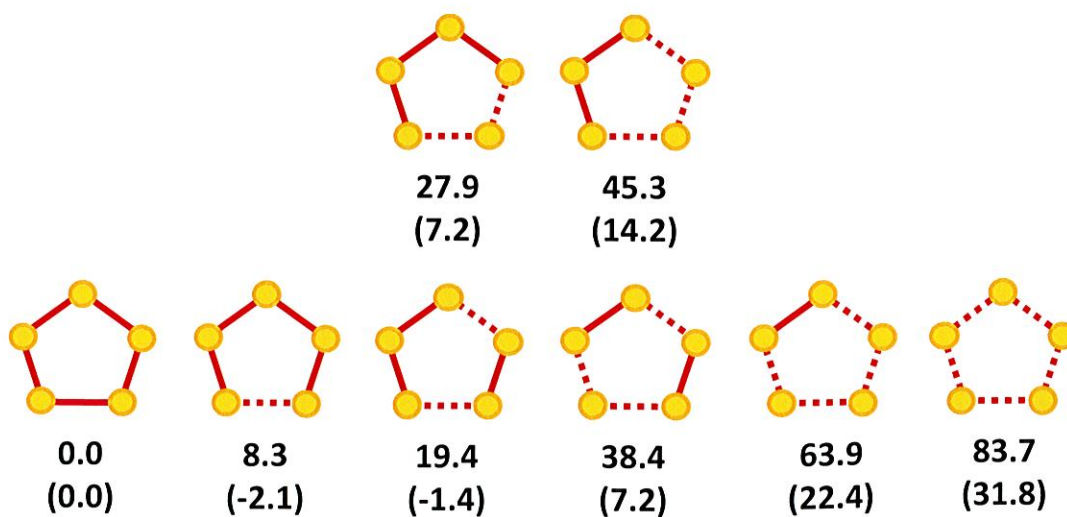


Figure 4. Speciation of pentagonal $[(U^{VI}O_2)_5(\eta^2-O_5)_5(\mu-\eta^2, \eta^2-O_2)_{5-n}(OH)_{2n}]^{10-}$ uranyl-peroxide nanocapsule building blocks at pH=14 and $[OOH^-]=1M$, and in parenthesis pH=8 and $[H_2O_2]=1mM$. Gibbs free energies in $kcal\ mol^{-1}$ relative to $[(U^{VI}O_2)_5(\eta^2-O_5)_5(\mu-\eta^2, \eta^2-O_2)_5]^{10-}$.

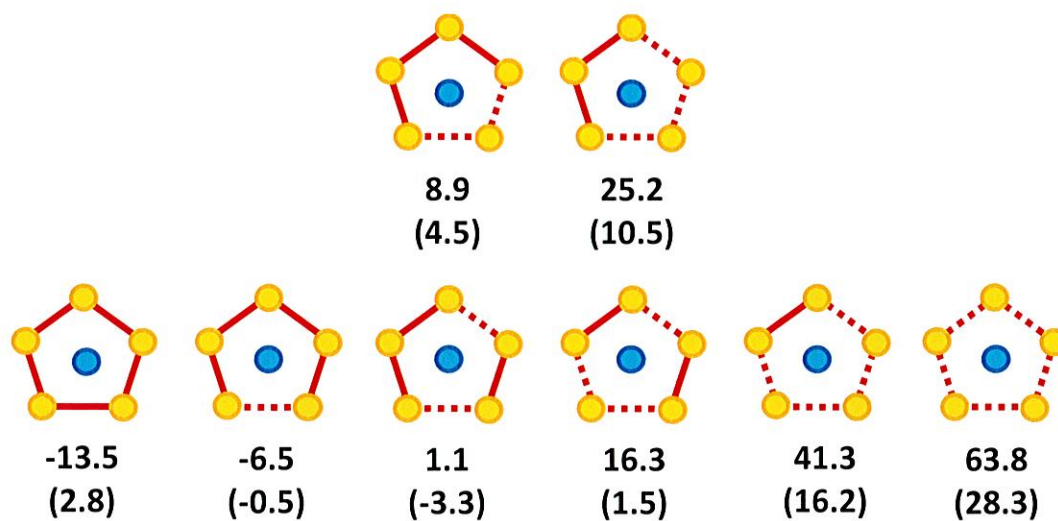


Figure 5. Speciation of pentagonal $[(U^{VI}O_2)_5(\eta^2-O_5)_5(\mu-\eta^2, \eta^2-O_2)_{5-n}(OH)_{2n}]^{10-}$ uranyl-peroxide nanocapsule building blocks in the presence of Na^+ at pH=14, $[Na^+]=1M$, and $[OOH^-]=1M$, and in parentheses pH=8, $[Na^+]=1mM$, and $[H_2O_2]=1mM$. Gibbs free energies in $kcal\ mol^{-1}$ relative to $Na[(U^{VI}O_2)_5(\eta^2-O_5)_5(\mu-\eta^2, \eta^2-O_2)_5]^{9-}$.

Electrostatic Potentials

After obtaining the optimized geometries for the $[(U^{VI}O_2)_5(\eta^2-O_5)(\mu-\eta^2,\eta^2-O_2)_5]^{10-}$ uranyl-peroxide species, we calculated the electrostatic potential for two of them: a full peroxide ($[(UO_2)_5(\eta^2-O_2)_5(\mu-\eta^2,\eta^2-O_2)_5]^{10-}$) and one with two sets of hydroxide bridges ($[(UO_2)_5(\eta^2-O_2)_5(\mu-\eta^2,\eta^2-O_2)_3(OH)_4]^{10-}$) (Figure 6). The electrostatic potential calculations showed that the uranyl oxygens were the most negative positions in the fully peroxide faces, but the hydroxide bridging was the most negative in the hydroxide faces. The counter cation coordinates with the faces in these positions to form an ion pair.

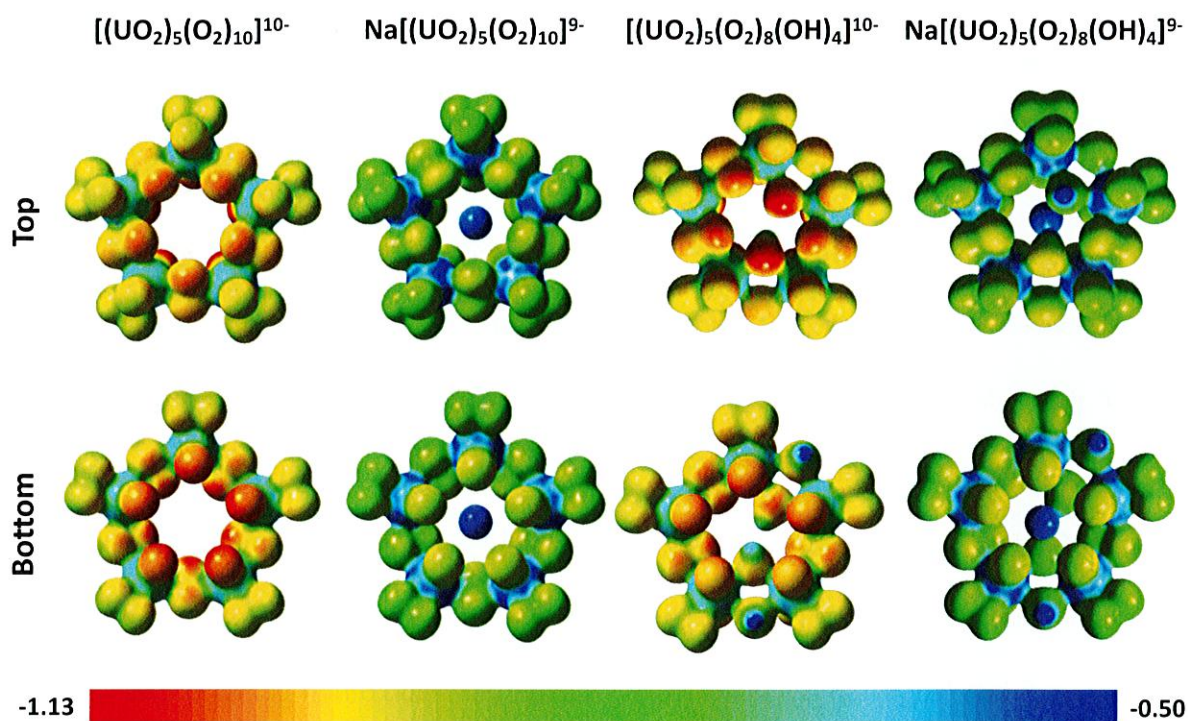


Figure 6. Electrostatic potential of $[(UO_2)_5(\eta^2-O_2)_5(\mu-\eta^2,\eta^2-O_2)_5]^{10-}$ and $[(UO_2)_5(\eta^2-O_2)_5(\mu-\eta^2,\eta^2-O_2)_3(OH)_4]^{10-}$ species with and without a Na^+ cation. Density isovalue = 0.04.

The analysis of the frontier orbitals of $[(UO_2)_5(\eta^2-O_2)_5(\mu-\eta^2,\eta^2-O_2)_5]^{10-}$ reveals two sets of five orbitals associated with the terminal and bridging peroxide ligands (Figure 7).

The top orbitals are the p^* antibonding orbitals of the terminal peroxide ligands, while the following set of orbitals are the p^* antibonding orbitals of the bridging peroxides.

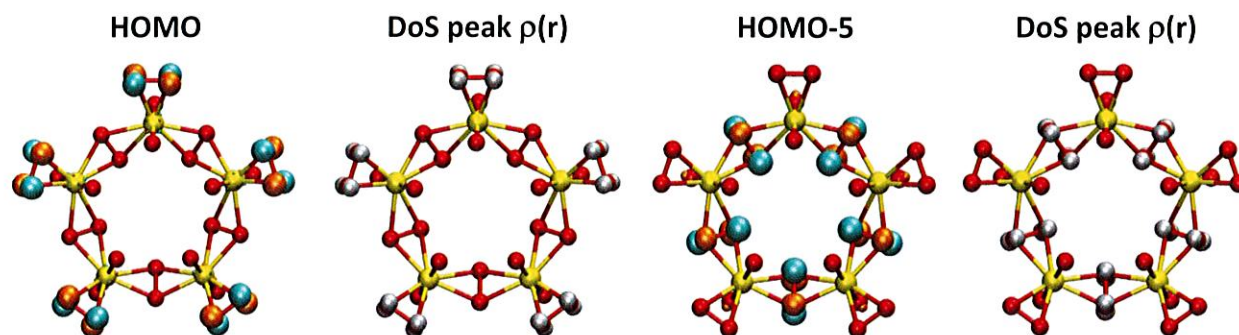


Figure 7. HOMO and HOMO-5 molecular orbitals for $[(UO_2)_5(\eta^2-O_2)_5(\mu-\eta^2, \eta^2-O_2)_5]^{10-}$ species and total density for the different DoS peroxide bands.

The plot of the density of states of the $[(U^{VI}O_2)_5(\eta^2-O_2)_5(\mu-\eta^2, \eta^2-O_2)_{5-n}(OH)_{2n}]^{10-}$ uranyl-peroxide species (Figure 8), further demonstrates this assignment. The peak associated with the bridging peroxides (<4 eV) systematically disappears with the replacement of bridging peroxides by hydroxides, while the terminal peroxide peak (>4 eV) remains mostly unchanged. These changes will also have implications on the Raman spectra of these species since peroxide is Raman active. The transformation of bridging peroxides into bridging hydroxides will reduce the peroxide Raman signal and it may be useful for the identification of structural changes in the species. In addition, the UV-Vis excitation energies from the peroxide/hydroxide orbitals to the empty uranium f-orbitals are also expected to be impacted.

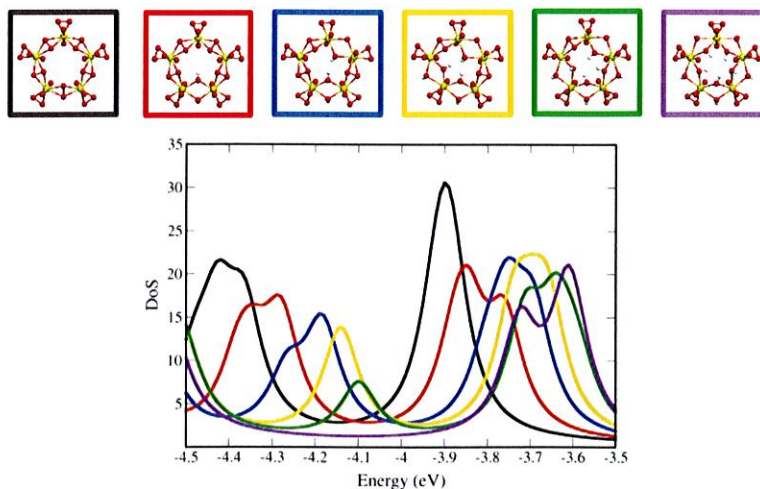


Figure 8. Density of states (DoS) for the frontier orbitals region of $[(U^{VI}O_2)_5(\eta^2-O_5)_5(\mu-\eta^2, \eta^2-O_2)_{5-n}(OH)_{2n}]^{10-}$ uranyl-peroxide species. Bridging peroxide bands are at <4 eV and terminal peroxide bands are at >4 eV.
Neural Network Potentials

The chemical space as well as many uranyl-peroxide nanoclusters are too large to be studied using quantum mechanics methods such as density functional theory. In consequence, computational bottom-up methodologies that thrive from leveraging quantum chemical results to build predictive models such as neural networks are essential as they can be used to complement previously used approaches and streamline the exploration of uranyl-peroxide chemical space. We mapped the potential energy surface by scanning the molecular normal modes and created a large database containing uranyl monomers $[(UO_2)(O_2)_3]^{4-}$ and $[(UO_2)(O_2)_2(OH)]^{3-}$. This approach maps the potential energy surface of a system displacing the ground state geometry along the harmonic normal modes (normal mode sampling). Neural network potentials derived from the potential energy surface mapping of uranyl-peroxide species can be used to create a structure-energy models capable of predicting quantum mechanics energetics and other properties at fraction of the computational cost.

Neural Network

We trained three NNPs using the atomistic machine-learning package (AMP): 1) using only the training data from the normal mode sampling of $[(\text{UO}_2)(\text{O}_2)_3]^{4-}$, 2) using only the training data from the normal mode sampling of $[(\text{UO}_2)(\text{O}_2)_2(\text{OH})]^{3-}$, and 3) using the training data from the normal mode sampling of both $[(\text{UO}_2)(\text{O}_2)_3]^{4-}$ and $[(\text{UO}_2)(\text{O}_2)_2(\text{OH})]^{3-}$. After the models were trained, we checked their performance with their test sets (Figures 9, 10, and 11) showing a very good agreement between the DFT (correct) and the predicted NNP energies.

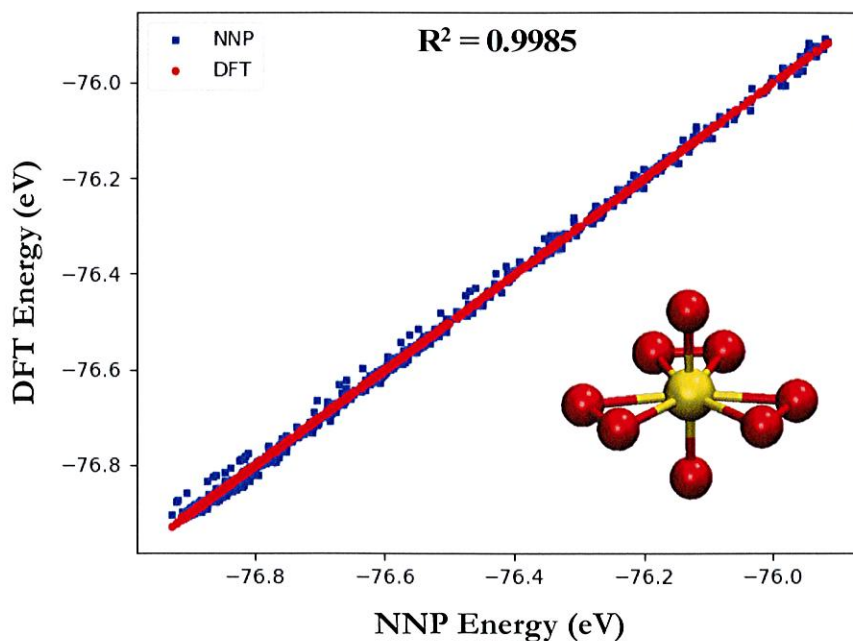


Figure 9. NNP vs DFT energy for the $[(\text{UO}_2)(\text{O}_2)_3]^{4-}$ test set. NNP was trained using only the training data from the normal mode sampling of $[(\text{UO}_2)(\text{O}_2)_3]^{4-}$.

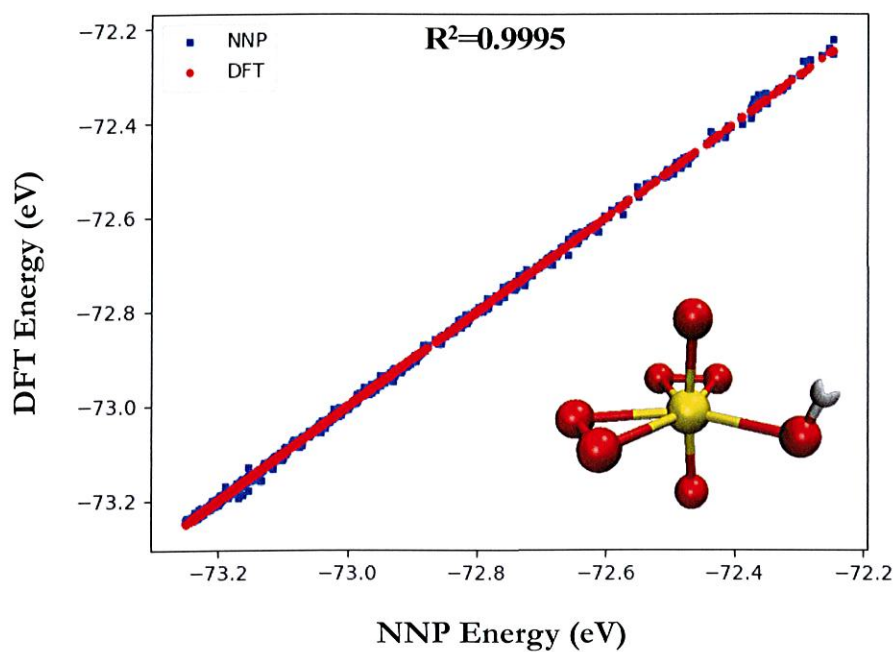


Figure 10. NNP vs DFT energy for the $[(\text{UO}_2)(\text{O}_2)_2(\text{OH})]^{3-}$ test set. NNP was trained using only the training data from the normal mode sampling of $[(\text{UO}_2)(\text{O}_2)_2(\text{OH})]$.

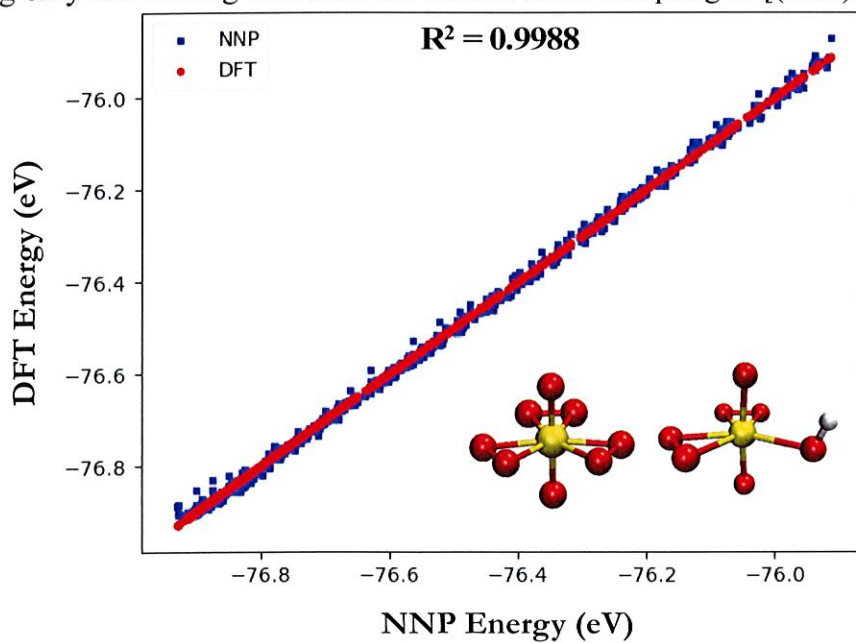


Figure 11. NNP vs DFT energy for the $[(\text{UO}_2)(\text{O}_2)_3]^{4-}$ and $[(\text{UO}_2)(\text{O}_2)_2(\text{OH})]^{3-}$ test set. NNP was trained using the training data from the normal mode sampling of both monomers.

The energetics of the NNPs are presented in Table 1 for the different species. The error between the DFT and NNP energy is below 1 kcal mol⁻¹ which is chemical accuracy. Furthermore, the trained NNP can be used to evaluate the energy of [(UO₂)(O₂)₃]⁴⁻ species over 2100% faster than DFT. These results are promising as it shows that it is possible to maintaining a high degree of accuracy for a fraction of the computational cost.

Table 1. Comparison between the DFT and NNP energies for different NNP models. Energies in kcal mol⁻¹.

Species	Training Set	DFT Energy	NNP Energy	Absolute Error
[(UO ₂)(O ₂) ₃] ⁴⁻	Itself	-1785.92	-1785.53	0.39
	Both	-1785.92	-1785.49	0.44

Finally, since the NNP contains information of the potential energy surface it can be used to predict the vibrational spectrum of [(UO₂)(O₂)₃]⁴⁻ and [(UO₂)(O₂)₂(OH)]³⁻ (Figure 12) The frequencies calculation is 20 times faster than quantum mechanics with errors in the order of 8 cm⁻¹. The spectra in Figure 12 are power spectra since the vibrational spectrum generated with the NNP spectra does include any selection rules. These results are highly promising, but their applicability is limited to the chemical space used in the training. The transferability of the NNP to larger species was not studied, but it is expected that with the addition of peroxide and hydroxide bridging species, NNP trained using small uranyl-peroxide species could be used to study large nanoclusters.

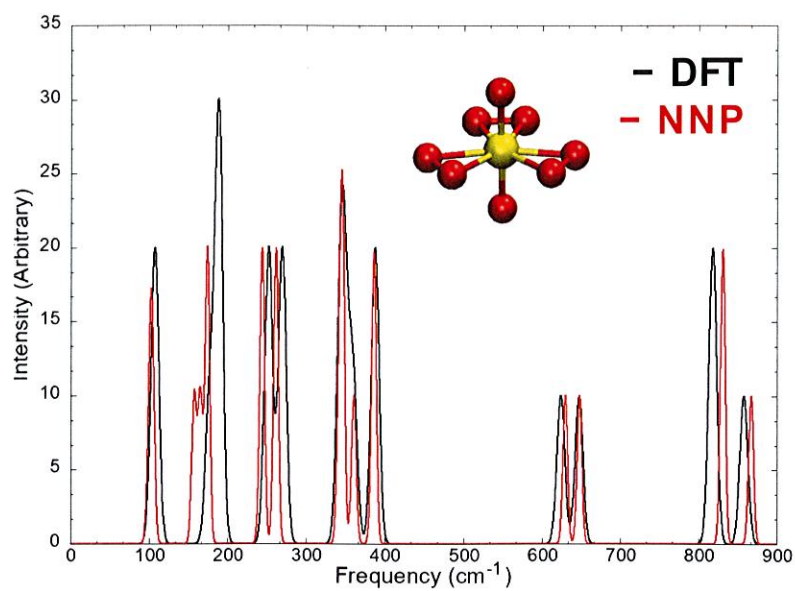


Figure 12. Power spectra from DFT (black) and NNP (red) for $[(\text{UO}_2)(\text{O}_2)_3]^{4-}$ species. NNP was trained using only the training data from the normal mode sampling of $[(\text{UO}_2)(\text{O}_2)_3]^{4-}$.

CHAPTER FOUR

Conclusions

In conclusion, we have studied the speciation pathways of the pentagonal faces with different number of peroxide and hydroxide ligands and at different experimental conditions. At very basic pH and high sodium and hydrogen peroxide concentration (pH=14, $[\text{Na}^+]=1\text{M}$, and $[\text{OOH}^-]=1\text{M}$), only the fully peroxide and singly hydroxide species are thermodynamically favorable. Under more mild conditions (pH=8, $[\text{Na}]=1\ \mu\text{M}$, and $[\text{H}_2\text{O}_2]=1\ \text{mM}$), favorability shifts towards the single and double hydroxide species. Importantly, as the species include additional bridging hydroxide ligands, a band in the density of states spectra disappears which may have applications in their spectral characterization.

In addition, we demonstrated a successful example of machine learning methods in calculating thermodynamic and spectroscopic properties of uranyl-peroxide species. The neural network potential calculates the energies of the uranyl-peroxide monomers two orders of magnitude faster and with a high degree of accuracy compared to conventional DFT methods. These results suggest a promising direction for machine learning in chemical systems, especially in larger uranyl-peroxide species.

REFERENCES

1. Nuclear Fuel Cycle Analysis and Management. In *Nuclear Reactor Physics and Engineering*, **2020**; pp 323.
2. Yoshida, N.; Kanda, J., Geochemistry. Tracking the Fukushima radionuclides. *Science* **2012**, *336* (6085), 1115.
3. Hoskin, P. W. O.; Burns, P. C., Ion exchange between aqueous fluid and spent nuclear fuel alteration products: Implications for the mobility of Cs in the probable repository at Yucca Mountain. *Mineralogical Magazine* **2018**, *67* (4), 689.
4. Armstrong, C. R.; Nyman, M.; Shvareva, T.; Sigmon, G. E.; Burns, P. C.; Navrotsky, A., Uranyl peroxide enhanced nuclear fuel corrosion in seawater. *Proceedings of the National Academy of Sciences of the United States of America* **2012**, *109* (6), 1874.
5. Christensen, H.; Sunder, S., Current State of Knowledge of Water Radiolysis Effects on Spent Nuclear Fuel Corrosion. *Nuclear Technology* **2017**, *131* (1), 102.
6. Kubatko, K. A.; Gunderson, K. M.; Antonio, M.; Burns, P. C.; Soderholm, L., Presence and persistence of uranyl peroxide nanoclusters in contact with geological media. *Materials Research Society Symposium Proceedings* **2006**, *893*, 387.
7. Burns, P. C.; Hughes, K.-A., Studtite, $[(UO_2)(O_2)(H_2O)_2](H_2O)_2$: The first structure of a peroxide mineral. *American Mineralogist* **2003**, *88* (7), 1165.
8. Kubatko, K. A. H.; Helean, K. B.; Navrotsky, A.; Burns, P. C., Stability of peroxide-containing uranyl minerals. *Science* **2003**, *302* (5648), 1191.
9. Qiu, J.; Burns, P. C., Clusters of actinides with oxide, peroxide, or hydroxide bridges. *Chemical Reviews* **2013**, *113* (2), 1097.
10. Burns, P. C.; Nyman, M., Captivation with encapsulation: a dozen years of exploring uranyl peroxide capsules. *Dalton Transactions* **2018**, *47* (17), 5916.
11. Wylie, E. M.; Peruski, K. M.; Weidman, J. L.; Phillip, W. A.; Burns, P. C., Ultrafiltration of Uranyl Peroxide Nanoclusters for the Separation of Uranium from Aqueous Solution. *ACS Applied Materials and Interfaces* **2014**, *6* (1), 473.
12. Miro, P.; Vlaisavljevich, B.; Gil, A.; Burns, P. C.; Nyman, M.; Bo, C., Self-Assembly of Uranyl-Peroxide Nanocapsules in Basic Peroxidic Environments. *Chemistry European Journal* **2016**, *22* (25), 8571-8578.

13. Miro, P.; Pierrefixe, S.; Gicquel, M.; Gil, A.; Bo, C., On the Origin of the Cation Templated Self-Assembly of Uranyl-Peroxide Nanoclusters. *Journal of the American Chemical Society* **2010**, *132* (50), 17787.
14. Vlasisavljević, B.; Gagliardi, L.; Burns, P. C., Understanding the Structure and Formation of Uranyl Peroxide Nanoclusters by Quantum Chemical Calculations. *Journal of the American Chemical Society* **2010**, *132* (41), 14503.
15. Qiu, J.; Vlasisavljević, B.; Jouffret, L.; Nguyen, K.; Szymanowski, J. E.; Gagliardi, L.; Burns, P. C., Cation templating and electronic structure effects in uranyl cage clusters probed by the isolation of peroxide-bridged uranyl dimers. *Inorganic Chemistry* **2015**, *54* (9), 4445.
16. Zanonato, P. L.; Di Bernardo, P.; Vallet, V.; Szabo, Z.; Grenthe, I., Alkali-metal ion coordination in uranyl(VI) poly-peroxide complexes in solution. Part 1: the Li^+ , Na^+ and K^+ -peroxide-hydroxide systems. *Dalton Transactions* **2015**, *44* (4), 1549.
17. Oliveri, A. F.; Colla, C. A.; Callahan, J. R.; Bogard, G.; Qiu, J.; Dembowski, M.; Burns, P. C.; Casey, W. H., Cation-Directed Isomerization of the U_{28} Uranyl-Peroxide Cluster. *European Journal of Inorganic Chemistry* **2017**, (46), 5429.
18. Gao, Y.; Dembowski, M.; Szymanowski, J. E. S.; Yin, W.; Chuang, S. S. C.; Burns, P. C.; Liu, T., A Spontaneous Structural Transition of $\{\text{U}_{24}\text{Pp}_{12}\}$ Clusters Triggered by Alkali Counterion Replacement in Dilute Solution. *Chemistry* **2017**, *23* (33), 7915.
19. *ADF 2017, SCM, Theoretical Chemistry, Vrije Universiteit, Amsterdam, The Netherlands*, <http://www.scm.com>.
20. te Velde, G.; Bickelhaupt, F. M.; Baerends, E. J.; Fonseca Guerra, C.; van Gisbergen, S. J. A.; Snijders, J. G.; Ziegler, T., Chemistry with ADF. *Journal of Computational Chemistry* **2001**, *22* (9), 931.
21. Van Lenthe, E.; Baerends, E. J., Optimized Slater-type basis sets for the elements 1–118. *Journal of Computational Chemistry* **2003**, *24* (9), 1142.
22. Perdew, J. P.; Burke, K.; Ernzerhof, M., Generalized Gradient Approximation Made Simple. *Physical Review Letters* **1996**, *77* (18), 3865.

23. Perdew, J. P.; Burke, K.; Ernzerhof, M., Generalized Gradient Approximation Made Simple [Phys. Rev. Lett. 77, 3865 (1996)]. *Physical Review Letters* **1997**, 78 (7), 1396.
24. van Lenthe, E.; Baerends, E. J.; Snijders, J. G., Relativistic total energy using regular approximations. *The Journal of Chemical Physics* **1994**, 101 (11), 9783.
25. van Lenthe, E.; Ehlers, A.; Baerends, E.-J., Geometry optimizations in the zero order regular approximation for relativistic effects. *The Journal of Chemical Physics* **1999**, 110 (18), 8943.
26. Klamt, A.; Schüürmann, G., COSMO: a new approach to dielectric screening in solvents with explicit expressions for the screening energy and its gradient. *Journal of the Chemical Society, Perkin Transactions 2* **1993**, (5), 799.
27. Khorshidi, A.; Peterson, A. A., Amp: A modular approach to machine learning in atomistic simulations. *Computer Physics Communications* **2016**, 207, 310.
28. Behler, J.; Parrinello, M., Generalized Neural-Network Representation of High-Dimensional Potential-Energy Surfaces. *Physical Review Letters* **2007**, 98 (14), 146401.